Journal of Metals, Materials and Minerals, 33(3), 1675, 2023

Biomass-based nitrogen-doped carbon/polyaniline composite as electrode material for supercapacitor devices

Krittaprot THONGKAM[1], Nattawut CHAIYUT[1], Manop PANAPOY[1,2], and Bussarin KSAPABUTR[1,2,*]

[1] *Department of Materials Science and Engineering, Faculty of Engineering and Industrial Technology, Silpakorn University, Sanamchandra Palace Campus, Nakhon Pathom, 73000, Thailand*

[2] *Center of Excellence on Petrochemical and Materials Technology, Chulalongkorn University, Bangkok, 10330, Thailand*

***Corresponding author e-mail:** ksapabutr_b@su.ac.th

Received date:
10 March 2023
Revised date
26 May 2023
Accepted date:
10 June 2023

Keywords:
Supercapacitor;
In-situ synthesis;
Polyaniline;
Nitrogen-doped activated carbon;
Water hyacinth

Abstract

Nitrogen-doped activated carbon (N-AC) was prepared from water hyacinth stems for loading polyaniline (PANI) by in-situ polymerization to synthesize N-AC/PANI composites for utilization as electrode materials in supercapacitors. Using potassium hydroxide as the activating agent, stems of water hyacinth were carbonized and activated in a single step to produce N-AC powders. Raman, FTIR, SEM, BET, TGA, and XPS techniques were used to characterize the resultant N-AC materials. The findings revealed that the N-AC materials had a porous structure and high specific surface area. Neat PANI was synthesized by varying the reaction time to 8, 16, and 24 h. During the reaction time of 16 h, the maximum specific capacitance was obtained. For the synthesis of N-AC/PANI composites, in-situ polymerization of aniline was performed for 16 h. Tests of cyclic voltammetry and galvanostatic charge/ discharge were conducted on the electrode materials to assess their electrochemical performance for supercapacitors. Because of the synergistic effect of PANI and N-AC, the produced N-AC/PANI composite showed good supercapacitor performance compared with neat PANI and N-AC. In the case of the N-AC/PANI composite, the specific capacitance was determined by the electrochemical double-layer capacitance (EDLC) of N-AC and the pseudocapacitance resulting from the redox reaction of PANI.

1. Introduction

The impact of environmental pollution has seriously restricted global sustainable development. Therefore, it is crucial to research components for clean, efficient, high-powered, and sustainable energy storage systems. Supercapacitors have garnered significant interest owing to their high-voltage energy storage properties, large energy storage capacity, and wide applications such as energy storage devices for various types of portable applications, solar energy, and electric vehicles [1-3]. Electrode materials are considered to be one of the most important variables influencing supercapacitor performance in energy storage. Conductive polymers are outstanding candidates as super-capacitor electrode materials. Polyaniline (PANI) has been extensively studied as an emerging electrode material of supercapacitors because of its large intrinsic redox states, pseudocapacitance, and ease of synthesis. However, the cycle life of PANI electrodes is usually poor because PANI volumetrically swells and shrinks during repeated charging and discharging cycles, leading to structural breakdown and rapid capacitance decay of PANI [4-5]. To promote the specific capacitance and cycling stability of PANI electrodes, researchers have focused on synthesizing and preparing composites with various carbon materials [6-8].

The carbon materials used to create carbon/PANI composites can act as conductive interfaces and have high surface areas, which facilitate de-doping and doping of counterions during the redox-influenced structural change of PANI. The porosity of carbon also has a substantial influence on the features of carbon/PANI composites by promoting fast ion transport and enhancing specific capacitance and stability. The incorporation of carbon materials into PANI is a useful method for improving the cycling durability and specific capacitance of PANI electrodes because of the synergistic combination of the large pseudocapacitance of PANI and the superior mechanical strength of the carbon materials [9,10]. Water hyacinth (WH), a type of floating plant, is native to the Amazon but can now be found worldwide in water systems. Recently, a great deal of research has suggested that a hierarchically organized three-dimensional (3D) porous structure with a large surface area derived from WH with activation can serve as an excellent template for supercapacitors [11,12]. It is noteworthy that WH has a well-designed hierarchical structure with three levels: millimeters, micrometers, and nanometers. Consequently, carbon materials derived from WH exhibit high surface areas, excellent electrical conductivities, and remarkable electro-chemical properties. Direct pyrolysis and carbonization of WH with potassium hydroxide as an activator can provide a hierarchical porous activated carbon (AC) matrix with commercial potential for use as an electrode. Positive characteristics for employing WH as a source of super- capacitors are the excellent electrochemical stability, abundance, and low cost of AC materials derived from WH [11-13]. Previous

reports have demonstrated that AC obtained from WH has a higher specific capacitance than that obtained from other biomasses, such as oil palm fruit, tobacco, corn stalk, onion, cattail, banana stem, rubber wood sawdust, and sago [11,12,14]. To improve the performance of AC supercapacitors, among the different doping approaches, N-type doping is regarded as one of the most effective ways because it can potentially improve the hydrophilic polar sites and electrical conductivity. In addition, nitrogen atoms in nitrogen-doped AC materials could function as redox-active centers, which could induce pseudocapacitance and increase the specific capacitance [15,16]. The most efficient method for N-doping is the direct reaction between a precursor and a nitrogen-rich material to obtain nitrogen-doped AC (N-AC).

In this study, melamine was chosen as the nitrogen source for N-doping because of its low price, easy availability, and high nitrogen percentage (67%). Furthermore, potassium hydroxide (KOH) is a popular activator capable of producing advanced porous structures under specific conditions [17,18] and was chosen as an activator for the preparation of N-AC. In most cases, carbon-based materials are used, but their charge storage mechanism based on electrochemical double-layer capacitors (EDLCs) results in relatively low capacitance. Therefore, a combination of EDLC and pseudocapacitive materials is required to achieve higher capacitance and stability [6]. In this work, N-AC was produced from WH stems for mixing with PANI by in-situ polymerization to synthesize N-AC/PANI composites for use as the electrode material of supercapacitors.

2. Experimental

2.1 Materials

Water hyacinth (WH) stems were obtained from Chachoengsao, Thailand. Potassium hydroxide (KOH) was procured from Carlo Erba Reagents S.A.S (France). Melamine (99%) was obtained from ACROS Organics (Poland). Aniline monomer was purchased from Loba Chemie Pvt. Ltd. (India). Ammonium persulfate ($(NH_4)_2S_2O_8$) was obtained from Ajax Finechem Pty. Ltd. (Poland). Sulfuric acid (H_2SO_4) was supplied from Quality Reagent Chemical (New Zealand). All of the reagents were employed without any additional purification.

2.2 Preparation of N-AC

The N-AC powders were produced from WH stems via a one-step carbonization-activation process. The WH stems were cleaned with water, sliced into tiny pieces, dried, and ground in a grinder. The dried WH powders were then mixed with KOH and melamine in a 1:1:1 ratio and carbonized at 700°C in an atmosphere of N2 for 1 h. The obtained material was washed, pH-neutralized, and dried at 70°C. In the next step, WH-derived N-AC was produced and sieved to achieve the desired particle size of 25 µm.

2.3 Synthesis of neat PANI and N-AC/PANI composite

A typical synthesis of neat PANI was carried out as follows: 0.1 mL of aniline was dissolved in a 1 M H_2SO_4 aqueous solution (25 mL) with stirring at 25°C for 30 min. An aqueous $(NH_4)_2S_2O_8$ solution was obtained by dissolving 0.25 g of $(NH_4)_2S_2O_8$ in 1 M H_2SO_4 (25 mL). Subsequently, the solution of $(NH_4)_2S_2O_8$ was gradually added to the aniline solution. The reaction times were varied at 8, 16, and 24 h. Therefore, the neat PANI samples obtained at different synthesis times were marked as PANI-8h, PANI-16h, and PANI-24h. To prepare the N-AC/PANI composite, N-AC (6 mg) was mixed with an aniline solution. The reaction mixture was then kept at 25°C and stirred for 16 h. The solution turned from black to dark green. The precipitates were washed with ethanol and distilled water before drying at 40°C for 24 h. The N-AC content was 14% by weight of the composite. The resulting composite was denoted as N-AC/PANI-16h. The mechanism of N-AC/PANI formation was shown in Figure S1.

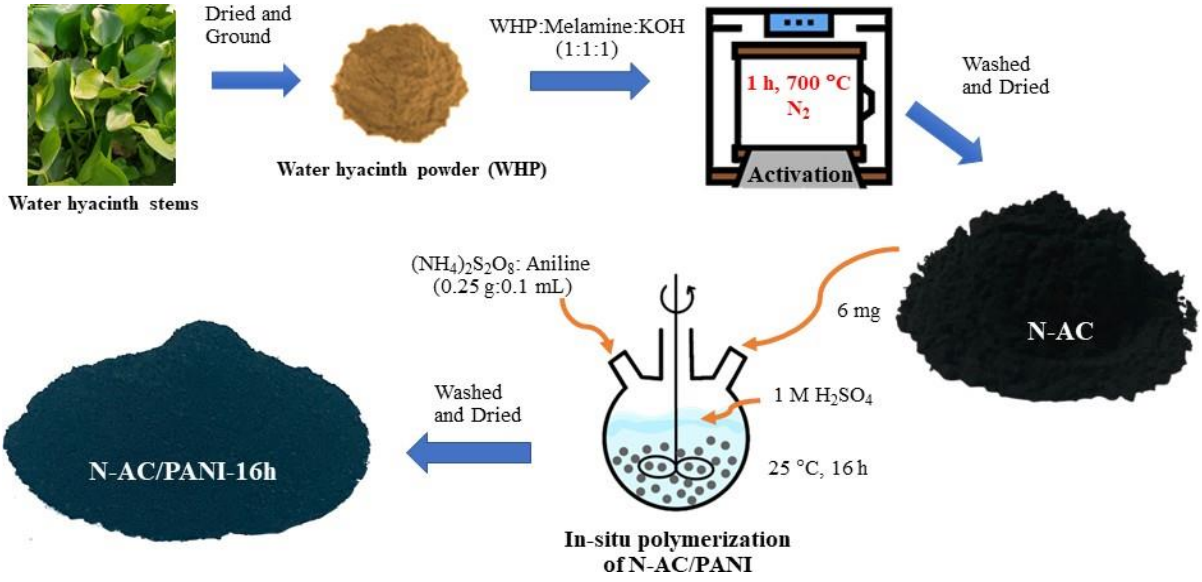

Figure 1. Schematic illustration of N-AC preparation and in-situ synthesis of N-AC/PANI composite

2.4 Material characterization

Raman spectra of N-AC, neat PANI, and N-AC/PANI composite were obtained using a Senterra Raman microscope (Bruker Optics Inc.). The surface functional groups of N-AC, neat PANI, and composite were studied using a Fourier transform infrared spectrometer (FTIR, Vertex 70, Bruker). Field-emission scanning electron microscopy (FESEM, MIRA3 Tescan) was employed to examine the sample surfaces and their morphologies. N2 adsorption and desorption were performed with a Micromeritics TriStar II 3020 apparatus to determine the BET surface area, pore size, and pore volume. A Perkin-Elmer thermogravimetric analyzer was used for thermogravimetric analysis (TGA). The temperature was increased from 30°C to 800°C at a heating rate of 10°C·min-1 under an N2 atmosphere. The sample compositions were determined using a Kratos AXIS Ultra X-ray photoelectron spectroscopy (XPS, Kratos Analytical Ltd.) with monochromatic Al-Kα radiation under a vacuum pressure of 10^{-9} Torr. The areas of peak were examined using CasaXPS software to fit the experimental data with Lorentzian-Gaussian curves. Relative sensitivity factors (RSFs) were used for the XPS quantification analysis. The atomic concentration (%) in each region was then determined.

2.5 Electrode preparation and electrochemical measurement

The electrodes were prepared using a mixed slurry consisting of 80% active material (N-AC, neat PANI, or N-AC/PANI composite), 15% acetylene black (AB50P, Polymaxx), and 5% poly(vinylidene fluoride) (PVDF, Sigma Aldrich). These materials were mixed with dimethylformamide (DMF) (Carlo Erba Reagents) until a homogeneous paste was formed. The resulting slurry was applied to a 1 cm² stainless steel wire mesh (SUS304) and dried overnight at 70°C. The mass loading was estimated to be 5 mg. A standard three-electrode cell configuration was employed to conduct the electrochemical analysis of the various electrodes. A silver chloride electrode (Ag/AgCl) and a platinum wire were used as the reference electrode and counter electrode, respectively. A 1 M solution of H2SO4 was used as the electrolyte. Cyclic voltammetry (CV) and galvanostatic charge/ discharge (GCD) investigations of the electrodes were conducted on an electrochemistry workstation (EA163, eDAQ, and ZIVE SP1). Electrochemical impedance spectroscopy (EIS) analysis was conducted over a frequency range from 100 kHz to 0.01 Hz with an AC voltage amplitude of 10 mV. The specific capacitance (Cs), energy density (E) and power density (P) of the electrodes were determined from the GCD plots using the following equations [19,20]:

$$C_s = \frac{I\Delta t}{m\Delta V} \quad (1)$$

$$E = \frac{C_s \Delta V^2}{8 \times 3.6} \quad (2)$$

$$P = 3600 \frac{E}{\Delta t} \quad (3)$$

Where Cs is the specific capacitance (F·g-1), E is the energy density (Wh·kg-1), P is the power density (W.·kg-1), I is the discharge current (A), Δt is the discharge time (s), m is the mass (g) of the active electrode material loaded onto the working electrode, and ΔV is the voltage window (V).

3. Results and discussion

Raman and FTIR analyses were conducted to investigate the chemical structure and composition of the as-prepared N-AC, synthesized PANI, and in-situ synthesized composite of N-AC/PANI. In Figure 2(a), the two broad peaks at approximately 1600 cm^{-1} and 1350 cm^{-1} in the Raman spectrum of N-AC coincide with the G and D peaks, which are associated with the typical sp2-hybridized carbon materials of carbon rings in N-AC, resulting from the ordered graphitic structure or defects in the graphitic structure, respectively [21]. Raman analysis of the PANI synthesized at different times and in-situ synthesized N-AC/PANI composite (Figure 2(a)) shows the prominent characteristic bands of PANI at 808 cm^{-1} (−NH−stretching), 1496 cm^{-1} (C=N stretching of the quinoid ring), and 1601 cm^{-1} (stretching of the benzenoid ring) [22,23]. Additionally, Raman characteristic peaks at 1170 cm^{-1} and 1330 cm^{-1} correspond to C−H bending in emeraldine and C−N^+ stretching of the polarons, respectively. These results indicated that both the neat PANI and PANI in the composite were in the conductive emeraldine form [21,24].

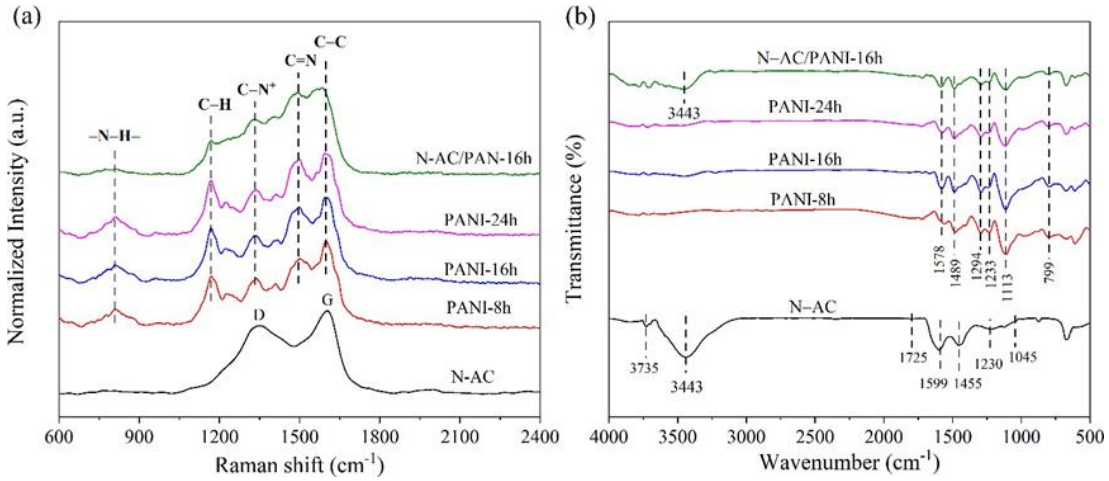

Figure 2. (a) Raman spectra and (b) FTIR spectra of N-AC, neat PANI samples synthesized at various times, and the N-AC/PANI composite materials.

The FTIR spectra of N-AC, neat PANI, and N-AC/PANI composite are displayed in Figure 2(b). The three intense bands of the N-AC sample at 1455, 1599, and 3443 cm^{-1} are assigned to the aromatic C=C bond, the NH bond, and the OH stretching of water, respectively [25]. A small peak at 1045 cm^{-1} and 1725 cm^{-1} observed in the spectrum of N-AC originates from the C–O and C=O bonds, respectively [26]. Furthermore, the low-intensity peaks at approximately 1230 cm^{-1} and 3735 cm^{-1} are sequentially associated with CN stretching and NH stretching vibrations [27,28]. These findings suggested that activated carbon contained nitrogen and oxygen atoms. Similar characteristic peaks can be seen in the FTIR spectra of both the N-AC/PANI composite and the neat PANI samples. The most prominent peaks of the PANI samples prepared at different times appear at around 1578, 1489, 1294, 1233, 1113, and 799 cm^{-1}. The peaks located at 1489 cm^{-1} and 1578 cm^{-1} were attributed to the C–C and C=C/C=N stretching vibrational modes of the benzenoid and quinoid rings, respectively. The C−N stretching of benzenoid and quinoid rings was also detected between 1233 cm^{-1} and 1294 cm^{-1}. The bands at 799 cm^{-1} and 1113 cm^{-1} indicate the out-of-plane and in-plane bindings for the C−H stretching of PANI, respectively [29,31]. Moreover, further XPS characterization confirmed their elemental compositions and chemical states of the elements, as shown in Figure 5.

The morphologies and microstructures of N-AC, neat PANI, and N-AC/PANI composite materials were investigated using FESEM. Figures 3(a-j) show the FESEM images of the PANI samples obtained at various synthesis times. The PANI-8h sample exhibited a three-dimensional (3D) interconnected rod-like structure (Figures 3(a-b)). As the in-situ synthesis time increased from 8 h to 16 h, PANI-16h became a 3D porous structure of PANI with web formation, as shown in Figures 3(c-d). Notably, when the synthesis time was extended to 24 h, the porous structure of PANI-24h decreased (Figures 3(e-f)). In the case of the N-AC/PANI-16h composite (Figures 3(g-h)), the N-AC surface was mainly covered by a 3D porous hierarchical structure with the web formation of PANI, which had a structure similar to that of PANI-16h, but the agglomeration structure was lower. Figures 3(i-j) show that N-AC had a porous structure without PANI web formation. These observations demonstrated that a 3D porous hierarchical structure with PANI web formation and a lower agglomeration structure in N-AC/PANI-16h might facilitate the electrolyte ion diffusion within the electrode [32].

Figures 4(a-e) show plots of the nitrogen adsorption/desorption isotherms and the pore size distribution of the obtained samples. According to these results, the BET surface areas (average pore diameters) of PANI-8h, PANI-16h, PANI-24h, N-AC, and N-AC/PANI-16h were calculated as 22.782 $m^2 \cdot g^{-1}$ (7.003 nm), 27.778 $m^2 \cdot g^{-1}$ (6.551 nm), 25.309 $m^2 \cdot g^{-1}$ (6.277 nm), 1,233.580 $m^2 \cdot g^{-1}$ (2.414 nm) and 51.205 $m^2 \cdot g^{-1}$ (3.823 nm), respectively. The synthesis time of PANI increased from 8 h to 16 h, and the surface area increased because of the 3D porous structure of PANI with web formation; however, when the time was increased to 24 h, the surface area decreased because of the decreased porous structure, as shown in the SEM results (Figure 3). Moreover, the surface area of the N-AC/PANI composite was greatly reduced compared with that of neat N-AC. Since the N-AC material was composited with PANI, this resulted in a significant reduction in the pore structure, as PANI obscured the N-AC pores. For comparison with neat PANI, the N-AC/PANI composite had a larger surface area than that of all neat PANI samples. These results are consistent with those previously reported [33,34]. The BET specific surface area might have increased because of the successful growth formation of the PANI webs on N-AC, as shown in the SEM results. However, the surface area of N-AC/PANI-16h was larger than that of all neat PANI samples. Based on the IUPAC classification, the hysteresis loop in the relative P/P0 range of 0.4-0.9 is a type IV isotherm with a hysteresis loop of type H1, implying that all neat PANI samples are mesoporous [35]. In comparison, the adsorption isotherms for N-AC/PANI-16h and N-AC were a combination of type I and type IV isotherms (IUPAC classification), suggesting the existence of both micropore and mesopore structures [36]. In addition, the micropore and total pore volumes of these materials were determined using the Barrett-Joyner-Halenda (BJH) analysis, as reported in Table 1. Mesopores and micropores may provide diffusion channels and transport for electrolyte ions, whereas micropores offer space for ion storage [37]. As a result, the N-AC/PANI-16h sample had a higher capacitance than the neat PANI sample (Figure 7(b)).

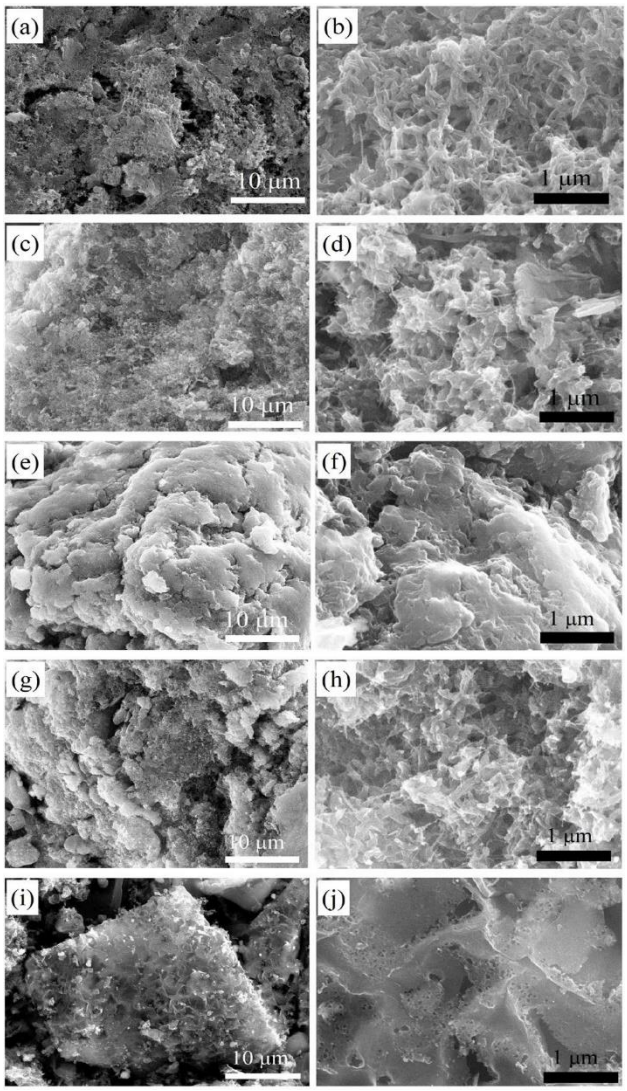

Figure 3. SEM images of neat PANI synthesized at various times: (a-b) PANI-8h, (c-d) PANI-16h, (e-f) PANI-24h, and SEM images of (g-h) N-AC/PANI-16h, (i-j) N-AC.

Table 1 The BET surface area and other characteristics of the synthesized samples.

Sample	S_{BET} ($m^2 \cdot g^{-1}$)	$S_{external}$ ($m^2 \cdot g^{-1}$)	S_{micro} ($m^2 \cdot g^{-1}$)	V_{total} ($cm^3 \cdot g^{-1}$)	V_{micro} ($cm^3 \cdot g^{-1}$)	Average pore diameter (nm)
N-AC	1,233.580	867.652	365.927	0.745	0.157	2.414
PANI-8h	22.782	22.782	-	0.039	-	7.003
PANI-16h	27.778	27.778	-	0.044	-	6.551
PANI-24h	25.309	25.309	-	0.043	-	6.277
N-AC/PANI-16h	51.205	40.370	10.835	0.049	0.005	3.823

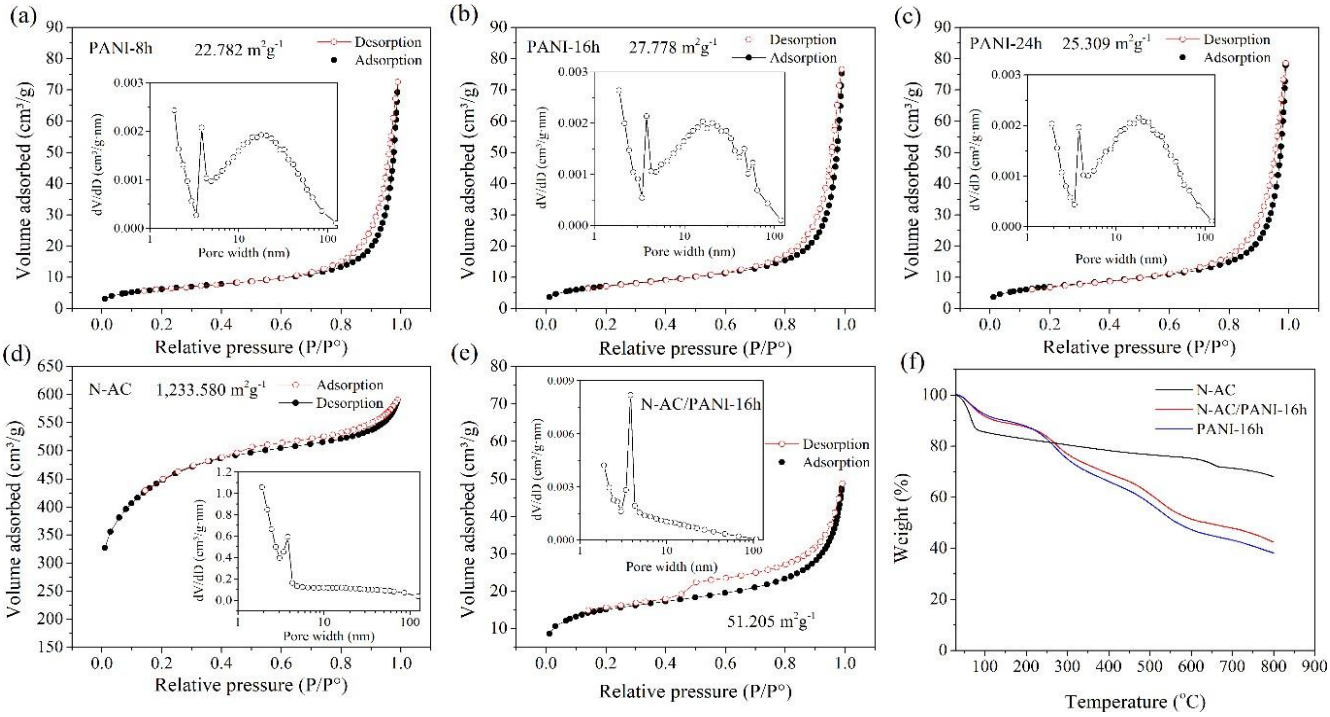

Figure 4. N2 adsorption/desorption isotherms (insets: the corresponding pore size distribution) of (a) PANI-8h, (b) PANI-16h, (c) PANI-24h, (d) N-AC, (e) N-AC/PANI-16h, and (f) TGA curves of N-AC, PANI-16h and N-AC/PANI-16h.

The thermal stabilities of the resulting samples were examined using TGA analysis. A nitrogen atmosphere was generated between 30°C and 800°C for heating the materials. The TGA thermograms in Figure 4(f) show that N-AC has better thermal stability than PANI-16h and N-AC/PANI-16h. The residual weight at 800°C was found to be 68, 38, and 42% for N-AC, PANI-16h, and N-AC/PANI-16h, respectively. The initial weight loss occurred at approximately 100°C owing to the vaporization of water molecules in the sample. The second step at ~140°C to 350°C was caused by the breakdown of functional groups containing oxygen resulting from the activation process. The last stage of decomposition at temperatures higher than 640°C might have resulted from the release of doped nitrogen [27]. In addition, three major weight losses were observed in the curves of PANI-16h and N-AC/PANI-16h. The first weight loss up to ~13°C corresponded to the water evaporation. The second weight loss occurred between 140°C and 350°C, which corresponds to the loss of oligomers and unreacted monomers in the samples. The further weight loss above 600°C was assigned to the thermal decomposition of PANI chains [38]. The N-AC/PANI-16h sample was slightly more thermally stable than the neat PANI-16h sample because of the existence of N-AC and the strong interactions between the PANI chains and N-AC particles [39].

In Figure 5(a), the XPS survey spectra show the chemical compositions of N-AC, PANI-16h, and N-AC/PANI-16h. Different peaks corresponding to O, N, and C elements were observed, supporting the presence of N elements on the surfaces of N-AC, PANI-16h, and N-AC/PANI-16h. The high-resolution N1s peaks of N-AC can be deconvoluted into four distinct types of oxidized pyridine nitrogen at 404.4 eV, quaternary nitrogen at 401.2 eV, pyrrolic nitrogen at 400.1 eV, and nitrogen subpeaks: pyridinic nitrogen at 398.7 eV (Figure 5(b)). In general, pseudocapacitive interactions occur on negatively charged pyrrolic nitrogen and pyridinic nitrogen. Meanwhile, the positively charged quaternary nitrogen and oxidized pyridine nitrogen could facilitate electron transfer through the carbon materials [40]. In addition, four peaks can be deconvoluted from the high-resolution spectrum of C1s for N-AC: C–C/C=C (284.8 eV), C–O (286.3 eV), C=O (289.2 eV), and C–N (285.6 eV), as shown in Figure S2. The presence of the C–N bond also indicated that N-AC was successfully doped with nitrogen atoms [15]. In Figures 5(c-d), the high-resolution N1s spectra of PANI-16h and N-AC/PANI-16h are split into three peaks at 400.5, 399.3, and 398.5 eV associated with the positively charged nitrogen (–NH+=), benzenoid amine (–NH–), and quinone imines (–N=), respectively. Benzenoid amines (–NH–) and quinone imines (–N=) contribute significantly to the

improvementin the specific capacitance of N doped materials because of their high pseudocapacitive properties. While the positively charged nitrogen (–NH+=) can increase the electrical conductivity of materials, which also enhances their electrochemical characteristics [41]. Table 2 shows the atomic percentages of the nitrogen species for PANI-16h and N-AC/PANI-16h determined from high-resolution XPS deconvolution. The atomic percentage of the sum of quinone imine (–N=) and benzenoid amine (–NH–) species for N-AC/PANI-16h (69.57 at%) was greater than that for PANI-16h (67.73 at%), indicating the high specific capacitance of N-AC/PANI-16h.

Cyclic voltammetry (CV) was performed to study the pseudo-capacitive behavior of all neat PANI, N-AC, and N-AC/PANI-16h electrodes in the applied voltage range from -0.2 V to +0.8 V in 1 M H_2SO_4 electrolyte at 10 mV·s-1 (Figure 6(a)). All neat PANI and N-AC/ PANI-16h electrodes showed double definite redox peaks, indicating the interconversion between the emeraldine and leucoemeraldine states of PANI. Additionally, a higher specific current was observed for the N-AC/PANI-16h electrode than for the neat PANI electrode. Therefore, the N-AC/PANI-16h composite electrode could have improved the specific capacitance and electrochemical performance. The neat PANI and N-AC/PANI-16h electrodes showed two distinguishable peaks, OI/RI (~0.30 V/~0.04 V) and OII/RII (~0.55 V/ ~0.40 V), resulting from the pseudocapacitance behavior of PANI. The N-AC/PANI-16h electrode had the greatest enclosed area, which indicated the highest specific capacitance. The N-AC/PANI-16h electrode showed a larger enclosed area than the neat PANI, suggesting that N-AC plays an essential role in increasing the specific capacitance and surface area of the N-AC/PANI-16h composite. The quasi-rectangular curve observed for N-AC demonstrates the existence of a double-layer capacitance mechanism (EDLC) [42]. Figure 6(b) shows the GCD curves of the N-AC, neat PANI, and N-AC/PANI-16h electrodes at a current density of 0.5 A·g-1. In the N-AC electrode, the GCD curves are nearly triangular in shape. In contrast, the neat PANI and N-AC/PANI-16h electrodes exhibited non-ideal straight lines, demonstrating the contribution of the pseudocapacitance from PANI. The specific capacitances calculated were 234, 269, 335, 314, and 431 $F \cdot g^{-1}$ for the N-AC, PANI-8h, PANI-16h, PANI-24h, and N-AC/ PANI-16h electrodes, respectively.

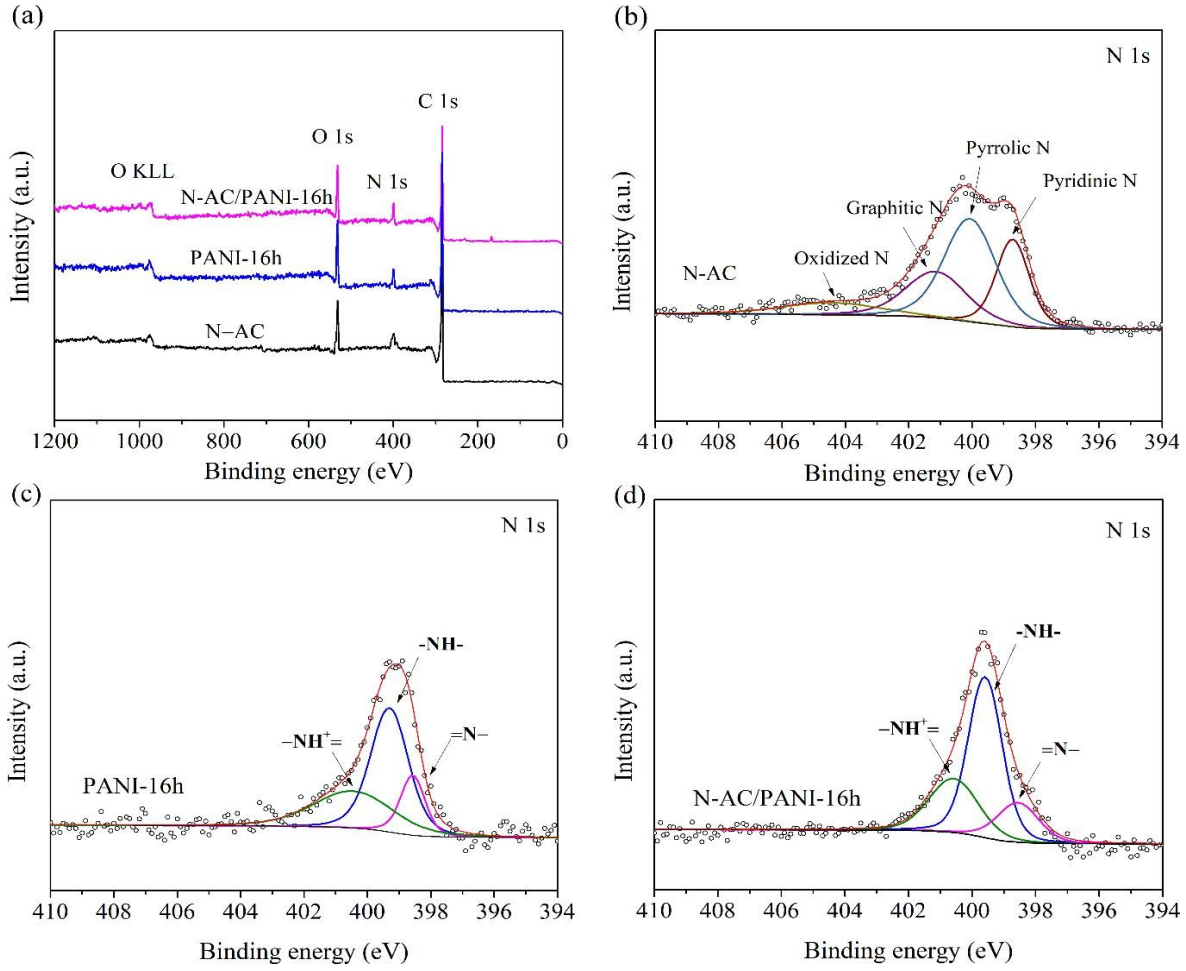

Figure 5. (a) XPS survey spectrum of N-AC, PANI-16h and N-AC/PANI-16h and high-resolution XPS spectra of N1s for (b) N-AC, (c) PANI-16h, and (d) N-AC/PANI-16h.

Table 2. Nitrogen species determined by XPS of PANI-16h and its composite.

Sample	Quinone imine (at%)	Benzenoid amine (at%)	Positively charged nitrogen (at%)
PANI-16h	16.02	51.71	32.27
N-AC/PANI-16h	11.37	58.2	30.42

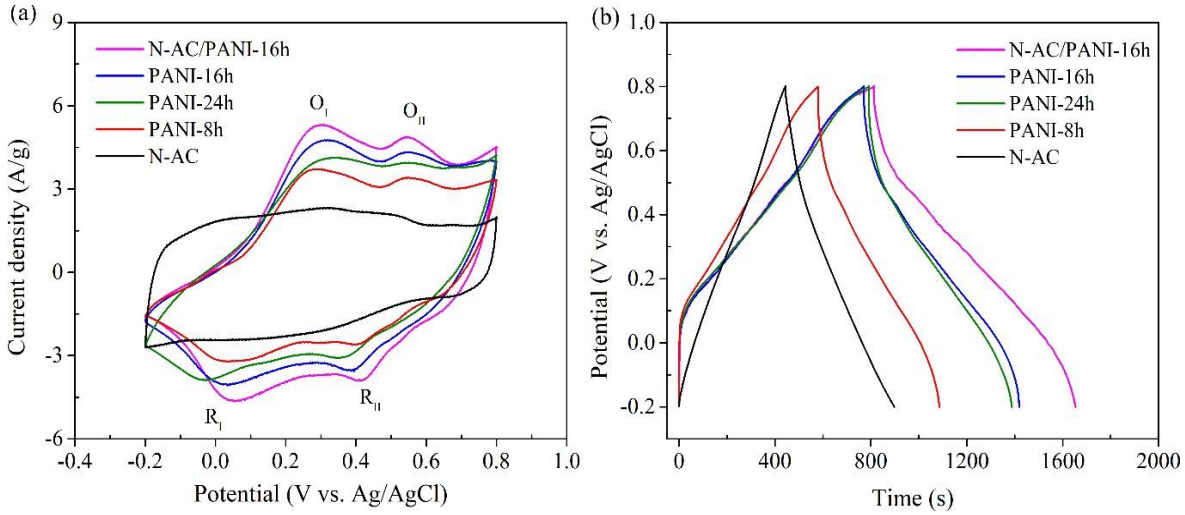

Figure 6. (a) CV curves of (a) N-AC, neat PANI and N-AC/PANI-16h at 10 $mV \cdot s^{-1}$ and (b) GCD curves of N-AC, neat PANI and N-AC/PANI-16h at the current density of 0.5 $A \cdot g^{-1}$.

The GCD curves of the N-AC/PANI-16h electrode at various current densities are presented in Figure 7(a). The noticeable plateaus indicate the presence of Faradaic redox reactions originating from the PANI. The charge/discharge curves for the N-AC/PANI-16h electrode show distinct plateaus at low current densities representing pseudocapacitive characteristics of N-AC/PANI-16h. Furthermore, the excellent reversible redox capacitance and Coulombic efficiency of the N-AC/PANI-16h electrode are also evident from the symmetrical GCD curves [9,43]. The specific capacitances at various current densities are demonstrated in Figure 7(b). The specific capacitance of each sample decreased with increasing current density. This could be because electrode pores are fully accessible at lower current densities, which results in greater charge storage and vice versa at higher current densities [44]. In addition, the N-AC/PANI-16h electrode showed specific capacitances at 0.5, 1, 2, 5, 10, and 20 $A \cdot g^{-1}$ of 431, 361, 296, 272, 248, 240, and 234 $F \cdot g^{-1}$, respectively. The specific capacitance of the N-AC/PANI-16h electrode was higher than that of all other electrodes, which gave the N-AC/PANI-16h superior performance over the individual electrodes of N-AC and neat PANI. Table S1 summarizes the specific capacitances of previously reported carbon-based supercapacitor electrodes [8,45-49]. Compared with previously reported electrodes, N-AC/PANI exhibited a higher specific capacitance. The higher specific capacitance can be attributed to the in-situ incorporation of N-AC into PANI and the 3D porous hierarchical structure of the PANI web, which has multiple electrochemically active sites.

To further examine the electrochemical behavior, EIS analysis was carried out for N-AC, PANI-16h, and N-AC/PANI-16h with Nyquist plots (Figure 8(a)). The equivalent circuit diagram of the EIS test was fitted using Zview software (inset in Figure 8(a)). The high- frequency intercept (Rs) reflects the solution resistances of 0.74, 0.95, and 0.87 Ω for the PANI- 16h, N-AC, and N-AC/PANI-16h electrodes, respectively. The appearance of a semicircle in the mid- to high-frequency range revealed the charge transfer resistance (Rct) at the electrode/electrolyte interface. Moreover, the Rct values for the PANI-16 h, N-AC, and N-AC/PANI-16h electrodes were 0.89, 0.98, and 0.81 Ω, respectively. In comparison with other electrode materials, the N-AC/PANI-16h electrode exhibited the lowest Rct value, resulting in an improved ion storage capacity and higher specific capacitance. The combination of in-situ incorporation of trace amounts of N-AC into PANI and a 3D porous hierarchical structure with PANI web formation containing multiple electrochemically active sites had the potential to significantly increase the charge transfer efficiency [43-50]. The straight line at the low-frequency range indicates the diffusion resistance (Warburg resistance (Rw)) of N-AC (1.34 Ω), PANI-16 h (4.98 Ω), and N-AC/PANI-16h (2.42 Ω). In Figure 8(b), the frequency-dependent analysis of complex capacitance reflects both the interfacial and bulk electrochemical characteristics. As a result, the electrode reached its maximum capacitance at low frequencies because the electrolyte ions had sufficient time to penetrate deeply into the interior of the porous electrode, thereby generating an abundance of faradaic reactions upon interacting with the surface- active sites. Electrolyte ions can only reach the exterior surfaces of electrodes at higher frequencies. Additionally, insufficient time intervals are available for slow faradaic charge storage, leading to a significant reduction in capacitance. The frequency dependence of the imaginary capacitance was analyzed using the relationship: $C'' = -Z'/\omega|z^2|$, resulting from the energy losses through irreversible processes (Figure 8(b)). Therefore, the present values showed that the electrode had a good ability for high power delivery in a short period of time, given that the relaxation time constant ($\tau 0$ ($1/f$max)) essentially represents the shortest time required to effectively deliver the stored energy [51]. The N-AC electrode had a small relaxation time constant (10 s), probably because of its larger surface area and smaller pore size [52], which enabled an increased rate of ion exchange at the interface of the electrode with the electrolyte in a 1 M H2SO4 aqueous electrolyte solution. It is possible that the N-AC/PANI-16h electrode charges faster than the PANI-16h electrode due to its lower relaxation time constant value [53]. Based on the porous structure and superior conductivity of the material, the rapid frequency response indicated that the supercapacitor showed rapid ion adsorption and diffusivity, as well as superior rate performance [54].

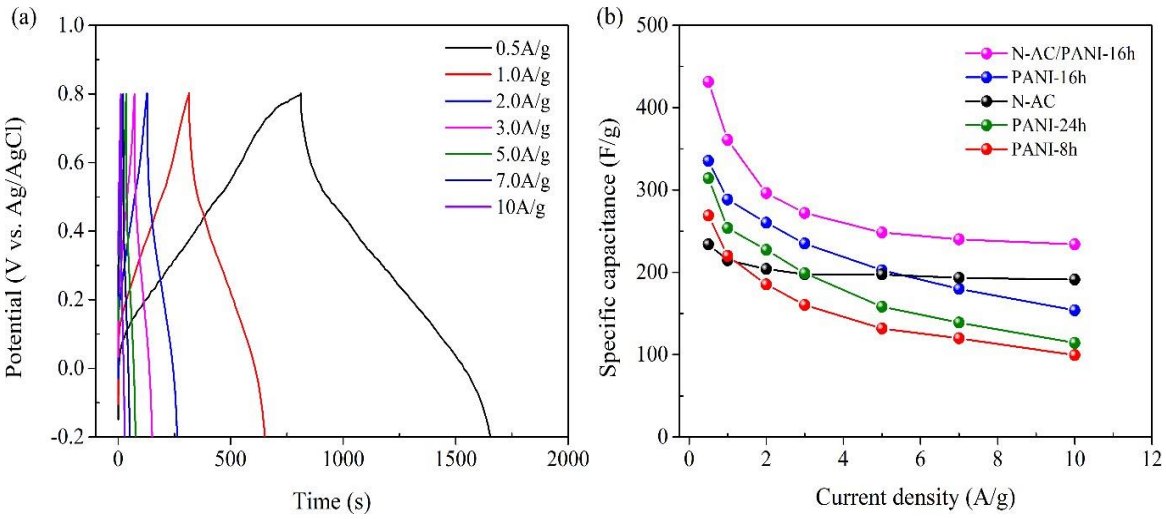

Figure 7. (a) GCD curves of the N-AC/PANI-16h electrode and (b) specific capacitance of N-AC, neat PANI and N-AC/PANI-16h at different current densities.

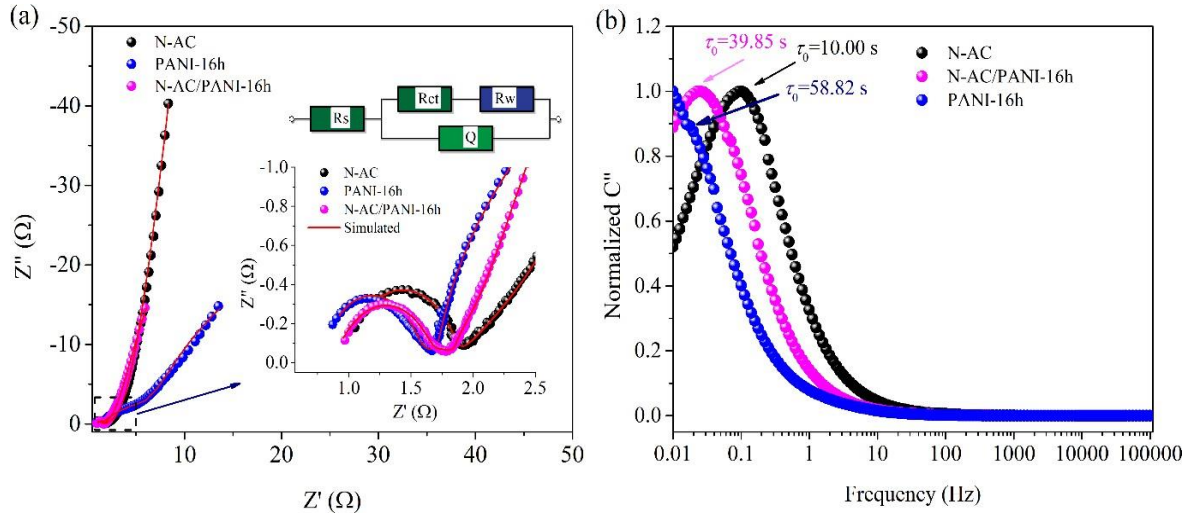

Figure 8. EIS measurements for the N-AC, PANI-16h and N-AC/PANI-16h electrodes: (a) Nyquist plots (inset is high frequency detail plots) and (b) frequency dependence of normalized imaginary capacitance.

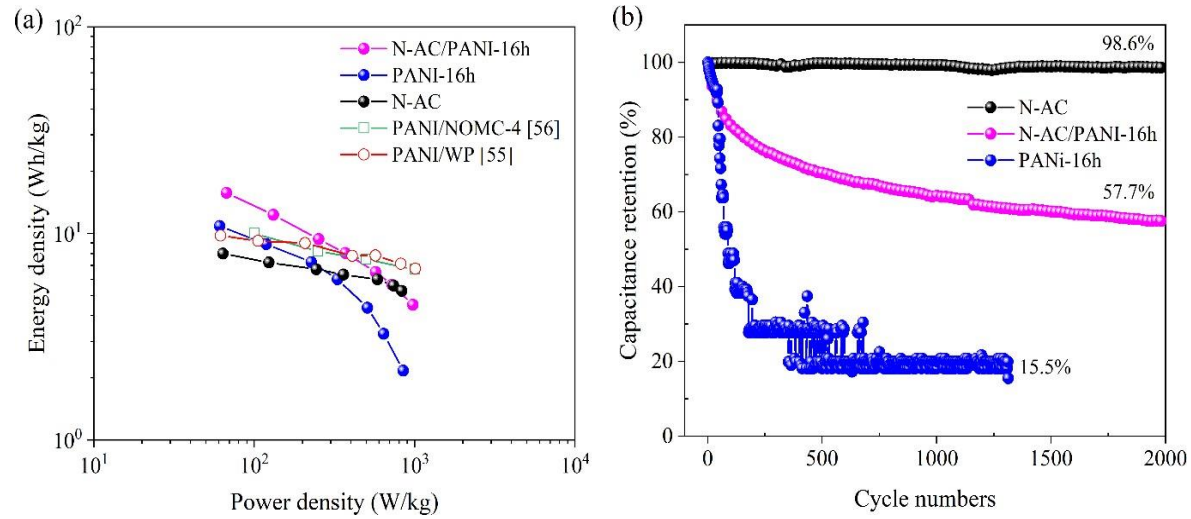

Figure 9. (a) Ragone plot of N-AC, PANI-16h, and N-AC/PANI-16h and comparison with the literature and (b) plot of % capacitance retention versus number of cycles.

Figure 9(a) is a Ragone diagram illustrating the relationship between energy density and power density of the designed supercapacitor at different current densities. The N-AC/PANI-16h electrode supercapacitor exhibited the maximum energy density of 15.73 $Wh{\cdot}kg^{-1}$ and the power density of 67.27 $W{\cdot}kg^{-1}$ at a current density of 0.5 $A{\cdot}g^{-1}$. At a current density of 20 $A{\cdot}g^{-1}$, the energy density remained high at approximately

4.52 $W{\cdot}kg^{-1}$ and the power density was 975.89 $W{\cdot}kg^{-1}$. Compared with N-AC and PANI-16h, N-AC/PANI-16h had greater energy density and power density. Thus, the in-situ composite of N-AC and PANI can improve the efficiency of supercapacitor electrodes. For practical applications, the cycling stability of supercapacitors is an essential characteristic. Moreover, the cycling stability of conductive polymerbased supercapacitors is one of the most significant challenges in producing low-cost electrode materials for commercial supercapacitors. Consequently, the cycling stability of the designed electrodes was examined by performing GCD measurements at a constant current density of 3 $A{\cdot}g^{-1}$. The PANI 16h electrodes showed a rapid decrease in capacitance with only approximately 20% capacitance retention after 1328 charge/discharge cycles, as depicted in Figure 9(b). PANI stores charges through fast surface redox reactions. During charging and discharging, this results in the swelling and shrinkage of the electrode materials. The electrode structure is eventually damaged by this ongoing physical change, which also leads to a loss of stability [6]. N-AC/PANI-16h showed superior cycling stability compared with PANI-16h and clearly demonstrated the significant contribution of N-AC in N-AC/PANI-16h with an excellent capacitance retention of 57.7% after 2000 GCD cycles. This could be attributed to the good interfacial bonding between N-AC and PANI in N-AC/ PANI-16h, which reduced the degradation of PANI during cycling [57].

4. Conclusions

This study described a simple method for synthesizing N-AC/PANI via in-situ polymerization. The characterization results revealed a well-designed 3D porous structure with PANI web formation grown on the porous 3D structure of N-AC. The N-AC/PANI-16h electrodes exhibited better electrochemical properties than neat PANI and N-AC. Additionally, in the galvanostatic charge/discharge studies, the highest specific capacity (431 $F{\cdot}g^{-1}$) was observed at a current density of 0.5 A.g-1. Thus, electron transport, ion transport, and cycling stability were enhanced in N-AC/PANI-16h compared with neat PANI because of its higher porous structure and good interaction between PANI and N-AC. The N-AC/PANI-16h electrode showed a maximum energy density of 15.73 $Wh{\cdot}kg^{-1}$ and a maximum power density of 975.89 $W{\cdot}kg^{-1}$. Consequently, the binary composite of N-AC and PANI could be considered as a promising and cost-effective material for supercapacitors with higher capacitance and longer cycle life.

Acknowledgements

The authors thank the Department of Materials Science and Engineering, Faculty of Engineering and Industrial Technology, Silpakorn University, and the Center of Excellence on Petrochemical and Materials Technology, Chulalongkorn University.

References

[1] R. T. Yadlapalli, R. R. Alla, R. Kandipati, and A. Kotapati, "Supercapacitors for energy storage: Progress, applications and challenges," *Journal of Energy Storage*, vol. 49, Article 104194, 2022.

[2] A. G. Olabi, Q. Abbas, A. A. Makky, and M. A. Abdelkareem, "Supercapacitors as next generation energy storage devices: Properties and applications," *Energy*, vol. 248, Article 123617, 2022.

[3] F. Bu, W. Zhou, Y. Xu, Y. Du, C. Guan, and W. Huang, "Recent developments of advanced micro-supercapacitors: Design, fabrication and applications," *npj Flex Electron*, vol. 4, Article 31, 2020.

[4] P. Jan, and S. Jaroslav, "Conductivity and morphology of polyaniline and polypyrrole prepared in the presence of organic dyes," *Synthetic Metals*, vol. 264, Article 116373, 2020.

[5] Y. Yu, A. Xu, Y. Zhang, W. Li, and Y. Qin, "Evaporation-induced hydrated graphene/polyaniline/carbon cloth integration towards high mass loading supercapacitor electrodes," *Chemical Engineering Journal*, vol. 445, Article 136727, 2022.

[6] D. J. Ahirrao, A. K. Pal, V. Singh, and N. Jha, "Nanostructured porous polyaniline (PANI) coated carbon cloth (CC) as electrodes for flexible supercapacitor device," *Journal of Materials Science & Technology*, vol. 88, pp. 168-182, 2021.

[7] H. N. Heme, M. S. N. Alif, S. M. S. M. Rahat, and S. B. Shuchi, "Recent progress in polyaniline composites for high capacity energy storage: A review," *Journal of Energy Storage*, vol. 42, no. May, p. 103018, 2021.

[8] W. Zhang, T. Xia, X. Huo, X. Li, S. Park, L. Lin, G. Diao, and Y. Piao, "Preparation of polyaniline/porous carbon spheres derived from γ-cyclodextrin for supercapacitors," *Journal of Electroanalytical Chemistry*, vol. 922, Article 116615, 2022.

[9] M. Ge, H. Hao, Q. Lv, J. Wu, and W. Li, "Hierarchical nano-composite that coupled nitrogen-doped graphene with aligned PANI cores arrays for high-performance supercapacitor," *Electrochimica Acta*, vol. 330, 2020.

[10] F. Fu, H. Wang, D. Yang, X. Qiu, Z. Li, and Y. Qin, "Lamellar hierarchical lignin-derived porous carbon activating the capacitive property of polyaniline for high-performance supercapacitors," *Journal of Colloid and Interface Science*, vol. 617, pp. 694-703, 2022.

[11] K. Zheng, Y. Li, M. Zhu, X. Yu, M. Zhang, L. Shi, and J. Cheng., "The porous carbon derived from water hyacinth with well- designed hierarchical structure for supercapacitors," *Journal of Power Sources*, vol. 366, pp. 270-277, 2017.

[12] Z. Zhang, Z. Gao, Y. Zhang, Z. Yan, I. Kesse, W. Wei, X. Zhao, and J. Xie, "Hierar-chical porous nitrogen-doped graphite from tissue paper as efficient electrode material for symmetric supercapacitor," *Journal of Power Sources*, vol. 492, Article 229670, 2021.

[13] V. Guna, M. Ilangovan, M. G. Anantha Prasad, and N. Reddy, "Water hyacinth: A unique source for sustainable materials and products," *ACS Sustainable Chemistry & Engineering*, vol. 5, no. 6, pp. 4478-4490, 2017.

[14] E. Taer, A. Afrianda, Apriwandi, R. Taslim, A. Agustino, Awitdrus, and R. Farma, "Production of activated carbon electrodes from sago waste and its application for an electro-chemical double-layer capacitor," *International Journal of Electrochemical Science*, vol. 13, pp. 10688-10699, 2018.

[15] T. Feng, S. Wang, Y. Hua, P. Zhou, G. Liu, K. Ji, Z. Lin, S. Shi, X. Jiang, and R. Zhang, "Synthesis of biomass-derived N, O-codoped hierarchical porous carbon with large surface area for high-performance supercapacitor," *Journal of Energy Storage*, vol. 44, pp. 1-11, 2021.

[16] B. J. Choudhury, H. H. Muigai, P. Kalita, and V. S. Moholkar, "Biomass blend de-rived porous carbon for aqueous super-capacitors with commercial-level mass loadings and enhanced energy density in redox-active electrolyte," *Applied Surface Science*, vol. 601, 2022.

[17] Q. Li, T. Lu, L. Wang, R. Pang, J. Shao, L. Liu, and X. Hu., "Biomass based N-doped porous carbons as efficient CO2 adsorbents and high-performance supercapacitor electrodes," *Separation and Purification Technology*, vol. 275, Article 119204, 2021.

[18] J. Sun, J. Zhang, M. Shang, M. Zhang, X. Zhao, S. Liu, X. Liu, S. Liu, and X. Yi., "N, O co-doped carbon aerogel derived from sodium alginate/melamine composite for all-solid-state supercapacitor," *Applied Surface Science*, vol. 608, Article 155109, 2023.

[19] T. C. Mendes, C. Xiao, F. Zhou, H. Li, G. P. Knowles, M. Hilder, A. Somers, P. C. Howlett, and D. R. MacFarlane, "In-situ- activated N-doped mesoporous carbon from a protic salt and its performance in supercapacitors," *ACS Applied Materials & Interfaces*, vol. 8, no. 51, pp. 35243-35252, 2016.

[20] W. Singsang, M. Panapoy, and B. Ksapabutr, "Facile one-pot synthesis of freestanding carbon nanotubes on cellulose-derived carbon films for supercapacitor applications: effect of the synthesis temperature," *Energy Procedia*, vol. 56, pp. 439-447, 2014.

[21] C. Ai, I. V. Chernyshova, E. L. Gawron, S. Ponnurangama, and V. I. Birss, "Electrochemistry of new generation conformal polyaniline/carbon scaffolds with monodispersed nanopores and high capacitance," *Journal of Materials Chemistry C*, vol. 10, pp. 2271-2280, 2022.

[22] A. V. Mohammadi, J. Moncada, H. Chen, E. Kayali, J. Orangi, C. A. Carrero, and M. Beidaghi, "Thick and freestanding MXene/PANI pseudocapacitive electrodes with ultrahigh specific capacitance," *Journal of Materials Chemistry A*, vol. 6, pp. 22123-22133, 2018.

[23] F. Fu, H. Wang, D. Yang, X. Qiu, Z. Li, and Y. Qin, "Lamellar hierarchical lignin-derived porous carbon activating the capacitive property of polyaniline for high-performance supercapacitors," *Journal of Colloid and Interface Science*, vol. 617, pp. 694-703, 2022.

[24] D. Shi, M. Yang, B. Zhang, H. Hu, Z. Ai, Y. Shao, J. Shen, Y. Wu, and X. Hao, "Design of boron carbonitrides-polyaniline (BCN-PANI) assembled supercapacitor with high voltage window," *Journal of Colloid and Interface Science*, vol. 626, pp. 544-553, 2022.

[25] S. Balou, S. E. Babak, and A. Priye, "Synergistic effect of nitrogen doping and ultra-Microporosity on the performance of biomass and microalgae-derived activated carbons for CO2 capture," *ACS Applied Materials & Interfaces*, vol. 12, pp. 42711-42722, 2020.

[26] Y. V. Fedoseeva , E. V. Lobiak., E. V. Shlyakhova, K. A. Kovalenko, V. R. Kuznetsova, A. A. Vorfolomeeva, M. A. Grebenkina, A. D. Nishchakova, A. A. Makarova, L. G. Bulusheva, and A. V. Okotrub, "Hydrothermal activation of porous nitrogen-doped carbon materials for electrochemical capacitors and sodium-ion batteries," *Nanomaterials*, vol. 10, no. 11, p. 1-19, 2020

[27] A. Aldalbahi, B. M. Thamer, M. Rahaman, and M. H. El-Newehy, "Self-nitrogen-doped nanoporous carbons derived from poly(1,5-diaminonaphthalene) for the removal of toxic dye pollutants from wastewater: Non-linear isotherm and kinetic analysis," *Polymers*, vol. 12, Article 2563, 2020.

[28] A. Zahoor, M. Christy, Y. J. Hwang, Y. R. Lim, P. Kim, and K. S. Nahm, "Improved electrocatalytic activity of carbon materials by nitrogen doping," *Applied Catalysis B*, vol. 147, pp. 633-641, 2014.

[29] S. Verma, D. S. Mal, P. R. D. Oliveira, B. C. Janegitz, J. Prakash, and R. K. Gupta, "A facile synthesis of novel polyaniline/ graphene nanocomposite thin films for enzyme-free electro- chemical sensing of hydrogen peroxide," *Molecular Systems Design & Engineering*, vol. 7, pp. 158-170, 2022.

[30] C. Wang, J. Ren, L. Zhou, Z. Li, L. Chen, and A. Zeng, "Interface growth of PANI-ZnO nanohybrids on a self-formed grapefruit peel aerogel to construct a quick self-Restored gas sensor," *ACS Synthetic Biology*, vol. 8, pp. 2483-2493, 2019.

[31] S. B. Teli, S. Molina, A. Sotto, E. G. Calvo, and J. D. Abajo, "Fouling resistant polysulfone−PANI/TiO_2 ultrafiltration nano-composite membranes," *Industrial Engineering Chemistry Research*, vol. 52, pp. 9470-9479, 2013.

[32] P. De, J. Halder, C. C. Gowda, S. Kansal, S. Priya, S. Anshu, A. Chowdhury, D. Mandal, S. Biswas, B. K. Dubey, and A. Chandra, "Role of porosity and diffusion coefficient in porous electrode used in supercapacitors-Correlating theoretical and experimental studies," *Electrochemical Science Advances*, pp. 1-15, 2022.

[33] L. Jin, Y. Jiang, M. Zhang, H. Li, L. Xiao, M. Li, and Y. Ao, "Oriented polyaniline nanowire arrays grown on dendrimer (PAMAM) functionalized multiwalled carbon nanotubes as supercapacitor electrode materials," *Scientific Reports*, vol. 8, no. 6268, pp. 1-10, 2018.

[34] G. Jiang, M. Chen, Y. Sun, and J. Pan, "Dual N-doped porous carbon derived from pyrolytic carbon black and critical PANIs constructing high-performance Zn ion hybrid supercapacitor," *Journal of Energy Storage*, vol. 63, Article 106955, 2023.

[35] M. Khosya, D. Kumar, M. Faraz, and N. Khare, "Enhanced photoelectrochemical water splitting and photocatalytic degradation performance of visible light active ZnIn2S4/PANI nanocomposite," *International Journal of Hydrogen Energy*, vol. 8, 2022.

[36] N. Mojoudi, N. Mirghaffari, M. Soleimani, H. Shariatmadari, C. Belver, and J. Bedia, "Phenol adsorption on high microporous

activated carbons prepared from oily sludge: equilibrium, kinetic and thermodynamic studies," *Scientific Reports*, vol. 9, no. 1, pp. 1-12, 2019.

[37] C. J. Verma, A. Kumar, S. Pal, S. Sinha, A. K. Singh, A. Jaiswal, and R. Prakash, "Polyaniline stabilized activated carbon from Eichhornia Crassipes: Potential charge storage material from bio-waste," *Renewable Energy*, vol. 162, pp. 2285-2296, 2020.

[38] M. Usman, M. Adnan, M. T. Ahsan, S. Javed, M. S. Butt, and M. Aftab Akram, "In situ synthesis of a polyaniline/ Fe–Ni co-doped Co_3O_4 composite for the electrode material of supercapacitors with improved cyclic stability," *ACS Omega*, vol. 6, pp. 1190-1196, 2021.

[39] P. Das, A. B. Deoghare, and S. Ranjan Maity, "Synergistically improved thermal sta-bility and electromagnetic interference shielding effectiveness (EMI SE) of in-situ synthe-sized polyaniline/sulphur doped reduced graphene oxide (PANI/S-RGO) nanocomposites," *Ceramics International*, vol. 48, no. 8, pp. 11031-11042, 2022.

[40] J. Cheng, Q. Xu, X. Wang, Z. Li, F. Wu, J. Shao, and H. Xie, "Ultrahigh-surface-area nitrogen-doped hierarchically porous carbon materials derived from chitosan and betaine hydrochloride sustainable precursors for high-performance supercapacitors," *Sustainable Energy Fuels*, vol. 3, pp. 1215-1224, 2019.

[41] W. Zhang, T. Xia, X. Huo, X. Li, S. Park, L. Lin, G. Diao, and Y. Piao, "Preparation of polyaniline/porous carbon spheres derived from γ-cyclodextrin for supercapacitors," *Journal of Electroanalytical Chemistry*, vol. 920, Article 116615, 2022.

[42] R. R. Atram, V. M. Bhuse, R. G. Atram, C. Wu, P. Koinkar, and S. B. Kondawar, "Novel carbon nanofibers/thionickel ferrite/polyaniline (CNF / $NiFe_2S_4$/PANI) ternary nanocomposite for high performance supercapacitor," *Materials Chemistry and Physics*, vol. 262, Article 124253, 2021.

[43] L. Xu, Y. Xi, W. Li, Z. Hua, J. Peng, J. Hu, J.-J. Zhou, P. Zhang, J. Wang, W. Wang, H. Ding, W. Wang, W. Ji, Y. Yang, X. Xu, L. Chen, and X. Li, "3D frame-like architecture of N- C-incorporated mixed metal phosphide boosting ultrahigh energy density pouch-type supercapacitors," *Nano Energy*, vol. 91, Article 106630, 2022.

[44] Manisha, M, Dhanda, R.Arora, A. S. Reddy, S. Lata, and A. Sharma, "Coalescing of lanthanum oxide and PPy @graphitic carbon nitride to achieve ultrahigh energy density electrode material for supercapacitors applications," *Journal of Alloys and Compounds*, vol. 955, Article 169738, 2023.

[45] Y. Meng, K. Wang, Y. Zhang, and Z. Wei, "Hierarchical porous graphene/polyaniline composite film with superior rate performance for flexible supercapacitors," *Advanced Materials*, vol. 25, no. 48, pp. 6985-6990, 2013.

[46] W. Tang, L. Peng, C. Yuan, J. Wang, S. Moa, C. Zhao, Y. Yu, Y. Min, and A. J. Epstein, "Facile synthesis of 3D reduced graphene oxide and its polyaniline composite for super capacitor application," *Synthetic Metals*, vol. 202, pp. 140-146, 2015.

[47] X. He, G. Liu, B. Yan, H. Suo, and C. Zhao, "Significant enhancement of electrochemical behaviour by incorporation of carboxyl group functionalized carbon nanotubes into polyaniline based supercapacitor," *European Polymer Journal*, vol. 83, pp. 53-59, 2016.

[48] S. K. Simotwo, C. Delre, and V. Kalra, "Supercapacitor electrodes based on high-purity electrospun polyaniline and polyaniline-carbon nanotube nanofibers," *ACS Applied Materials and Interfaces*, vol. 8, no. 33, pp. 21261-21269, 2016.

[49] N. Song, W. Wang, Y. Wu, D. Xiao, and Y. Zhao, "Fabrication of highly ordered polyaniline nanocone on pristine graphene for high-performance supercapacitor electrodes," *Journal of Physics and Chemistry of Solids*, vol. 115, pp. 148-155, 2018.

[50] G. Singh, Y. Kumar, and S. Husain, "Improved electrochemical performance of symmetric polyaniline/activated carbon hybrid for high supercapacitance: Comparison with indirect capacitance," *Polymers for Advanced Technologies*, vol. 32, pp. 4490-4501, 2021.

[51] C. Romanitan, P. Varasteanu, I. Mihalache, D. Culita, S. Somacescu, R. Pascu, E. Tanasa, S. A. V. Eremia, A. Boldeiu, M. Simion, A. Radoi, and M. Kusk, "High-performance solid-state supercapacitors assembling graphene interconnected networks in porous silicon electrode by electrochemical methods using 2,6-dihydroxynaphthalen," *Scientific Reports*, vol. 8, Article 9654, 2018.

[52] R. Harmas, R. Palm M. Harmas, M. Pohl, H. Kurig, I. Tallo, E. Tee, I. Vaas, R. Vali, T. Romann, O. Oll, R. Kanarbik, K. Liivand, J. Eskusson, J. Kruusma, T. Thomberg, A. Janes, P. Miidla, and E. Lust, "Influence of porosity parameters and electrolyte chemical composition on the power densities of non-aqueous and ionic liquid based supercapacitors," *Electrochimica Acta*, vol. 283, pp. 931-948, 2018.

[53] S. B. Mujib, F. Ribot, C. Gervais, and G. Singh, "Self-supporting carbon-rich SiOC ceramic electrodes for lithium-ion batteries and aqueous supercapacitors," *RSC Advances*, vol. 11, pp. 35440-35454, 2021.

[54] Y. Su, Z. Lu, J. Cheng, X. Zhao, X. Chen, and L. Gao, "Insulation board-derived N/O self-doped porous carbon as electrode materials for high-performance symmetric supercapacitor," *New Journal of Chemistry*, vol. 45, pp. 17503-17512, 2021.

[55] B. X. Zou, Y. Liang, X. X. Liu, D. Diamond, and K. T. Lau, "Electrodeposition and pseudocapacitive properties of tungsten oxide/polyaniline composite," *Journal of Power Sources*, vol. 196, pp. 4842-4848, 2011.

[56] K. Xie, M. Zhang, Y. Yang, L. Zhao, and W. Qi, "Synthesis and supercapacitor performance of polyaniline/nitrogen-doped ordered mesoporous carbon composites," *Nanoscale Research Letters* vol. 13, Article 163, 2018.

[57] D. Thanasamy, D. Jesuraj, V. Avadhanam, K. Chinnadurai, and S. K. K. Kannan, "Microstructural effect of various polyaniline-carbon nanotube core-shell nanocomposites on electrochemical supercapacitor electrode performance," *Journal of Energy Storage*, vol. 53, Article 105087, 2022.